The effect of spatial resolution
on magnetic field modeling and helicity computation

J. K. Thalmann[1], Manu Gupta[1], and A. M. Veronig[1,2]

[1] University of Graz, Institute of Physics/IGAM, Universitätsplatz 5, 8010 Graz, Austria e-mail: `julia.thalmann@uni-graz.at`
[2] Kanzelhöhe Observatory for Solar and Environmental Research, University of Graz, Austria

ABSTRACT

Context. Nonlinear force-free (NLFF) modeling is regularly used in order to indirectly infer the 3D geometry of the coronal magnetic field, not accessible on a regular basis by means of direct measurements otherwise.
Aims. We study the effect of binning in time series NLFF modeling of individual active regions (ARs) in order to quantify the effect of a different underlying spatial resolution on the quality of modeling as well as on the derived physical parameters.
Methods. We apply an optimization method to sequences of Solar Dynamics Observatory (SDO) Helioseismic and Magnetic Imager (HMI) vector magnetogram data at three different spatial resolutions for three solar active regions to obtain nine NLFF model time series. From the NLFF models, we deduce active-region magnetic fluxes, electric currents, magnetic energies and relative helicities, and analyze those with respect to the underlying spatial resolution. We calculate various metrics to quantify the quality of the derived NLFF models and apply a Helmholtz decomposition to characterize solenoidal errors.
Results. At a given spatial resolution, the quality of NLFF modeling is different for different ARs, as well as varies along of the individual model time series. For a given AR, modeling at a given spatial resolution is not necessarily of superior quality compared to that performed at different spatial resolutions at all time instances of a NLFF model time series. Generally, the NLFF model quality tends to be higher at reduced spatial resolution with the solenoidal quality being the ultimate cause for systematic variations in model-deduced physical quantities.
Conclusions. Optimization-based modeling based on binned SDO/HMI vector data delivers magnetic energies and helicity estimates different by ≲30%, given that concise checks ensure the physical plausibility and high solenoidal quality of the tested model. Spatial-resolution induced differences are relatively small compared to that arising from other sources of uncertainty, including the effects of applying different data calibration methods, those of using vector data from different instruments, or those arising from application of different NLFF methods to identical input data.

Key words. Sun: corona – Sun: magnetic fields – Methods: data analysis – Methods: numerical

1. Introduction

To date, the use of three-dimensional (3D) models of the coronal magnetic field is common practice, in order to obtain insights into related physical processes (Wiegelmann et al. 2017). Corresponding modeling approaches are needed due to the otherwise sparse direct measurements of the coronal magnetic field vector even within limited coronal volumes (e.g. review by Cargill 2009). In particular, nonlinear force-free (NLFF) magnetic field models are most often used (for dedicated reviews see, e.g., Wiegelmann & Sakurai 2012; Régnier 2013) which are static approximations of the magnetized coronal plasma being necessarily in equilibrium when the Lorentz force vanishes, i.e., when gas pressure and other forces are negligible. These conditions are satisfied to a high degree in the active-region corona (e.g., Gary 2001).

The computation of a force-free magnetic field, B, requires the numerical solution of

$$(\nabla \times B) \times B = \mathbf{0}, \tag{1}$$

and

$$\nabla \cdot B = 0, \tag{2}$$

within a 3D volume, V, subject to conditions specified on the model volume's lower boundary at $z = 0$. In other words, the

magnetic field information at the model's lower boundary is "extrapolated" into the coronal volume above. Ideally, in order to specify suitable boundary conditions to solve Eqs. (1)–(2), one would wish to have spectro-polarimetric observations at hand, that would allow to deduce a corresponding magnetic field vector consistent with the force-free assumption, for instance measured at chromospheric heights (e.g., Metcalf et al. 1995). In practice, however, such data at high spatial and temporal resolution are obtained only from measurements at photospheric heights. The latter are known to represent a regime inconsistent with the force-free approach because of non-negligible gas pressure and gravitational forces. Force-free modeling carried out on the basis of such inconsistent data is known to result in larger residual Lorentz force and divergence, yet may be partially compensated by, e.g., preprocessing of the photospheric vector data prior to extrapolation (e.g., Wiegelmann et al. 2006; Fuhrmann et al. 2011), the allowance of the force-free solution to deviate from the actually supplied input data at $z = 0$ (e.g, Wiegelmann & Inhester 2010; Wheatland & Régnier 2009; Wheatland & Leka 2011), or both (Wiegelmann et al. 2012).

In any case, force-free modeling at the full available spatial and temporal scales may be numerically expensive. Thus, to realize the modeling of, e.g., active regions (ARs) during their disk passage within a reasonable amount of time, the photospheric

vector magnetic field data are often spatially binned prior to their usage. DeRosa et al. (2015) provided the first comprehensive study on the effect of spatial resolution on NLFF modeling by testing the effect of binning of *Hinode*/SOT (Tsuneta et al. 2008; Lites et al. 2013) Stokes spectra onto the model outcome of five different numerical methods. In particular, they binned the Stokes spectra from a particularly chosen spectral scan of AR 10978 using nine different integer factors. Those nine spectra were then supplied to spectro-polarimetric inversion, 180°-ambiguity resolution, and remapping to a planar grid, ultimately representing the input data for subsequent NLFF modeling. Correspondingly, the employed single-snapshot models were at nine different spatial resolutions with plate scales ranging from ~0.1 Mm to ~1.7 Mm.

In order to obtain a more differentiated picture regarding the effect of spatial resolution onto NLFF modeling, we perform a corresponding in-depth analysis using one of the numerical methods compared in DeRosa et al. (2015), namely the optimization method of Wiegelmann et al. (2012), widely applied within the solar community for the purpose of coronal magnetic field modeling. In contrast to earlier studies, we do not base our analysis on a single-snapshot NLFF model of a single AR, but instead use time series of NLFF models during extended periods of time for different ARs (Sect. 2.1). This setting allows us, on the one hand, to explore in great detail the potential of known metrics to quantify the quality of NLFF solutions (Sect. 3.1). On the other hand, we may explore the effect of spatial resolution on the derived quantities, including magnetic fluxes and currents in 2D as well as energies and helicities in 3D (Sect. 3.2). Especially the analysis of magnetic helicity, a quantity characterizing the structural complexity of the magnetic field (e.g., Moffatt 1969), has recently gained much attention, as well as its sensitivity to the quality of the underlying magnetic field model (Valori et al. 2012; Thalmann et al. 2019, 2020). Ultimately, the employed sequences of NLFF models for several ARs allow us to deduce and discuss resolution-dependent trends (Sect. 4), and to compare those to other effects known to cause uncertainties in coronal magnetic field modeling (instrumental, data processing, etc.).

2. Data and Methods

2.1. Active region selection

For our study, we select three out of the 10 ARs analyzed in Gupta et al. (2021), namely NOAAs 11158, 11429 and 12673 which hosted the top four solar flares (in terms of peak soft X-ray flux) during solar cycle 24 that occurred within ±35° off the central meridian (see Table 1). The time window for analysis is chosen as in Gupta et al. (2021), i.e., covers a time interval of several hours around the occurrence of the X-class flares, as is the time cadence (a 12-min time cadence within ±1 hour around the flare peak time and a 1-hour cadence otherwise). Data possibly available during the flares' impulsive phases were not considered due to the limited validity of the force-free assumption during eruptive processes. Accordingly, the number of considered snapshots is different for each of the target ARs, based on the number of X-class flares within the analysis time window and also affected by the availability photospheric vector magnetic field data needed as an input for the analysis.

2.2. Vector magnetic field data

We use time series of vector magnetic field data as originally prepared by Gupta et al. (2021), who use HMI.SHARP_CEA_720s

Table 1. Properties of active regions under study, including NOAA number, GOES SXR class of X-class flares that occurred during the analysis time window and their respective on-disk location, followed by the number of vector magnetic field maps used.

NOAA AR no.	Flare class	Flare location	Analysis time window (UT) (YYYY-MM-DD hh:mm – DD hh:mm)	No. of maps
11158	X2.2	S20W10	2011-02-14 19:59 – 15 02:59	17
11429	X5.4	N18E31	2012-03-06 18:59 – 07 02:23	26
12673	X2.2	S08W32	2017-09-06 02:59 – 06 12:47[a]	22
	X9.3	S09W34		

Notes. [a] No SDO/HMI data available between 06 Sep 06:00 UT and 08:48 UT.

data within automatically identified active-region patches (Bobra et al. 2014), constructed from polarization measurements of the Helioseismic and Magnetic Imager (HMI; Scherrer et al. 2012) on board the Solar Dynamics Observatory (SDO; Pesnell et al. 2012), and projected onto a (local) heliographic plane (Gary & Hagyard 1990). Besides using time series of photospheric vector magnetic field data at a native plate scale (0.36 Mm at disk center; hereafter called "bin1"), we construct corresponding "bin2" and "bin4" time series by binning the original-resolution data by a factor of 2 and 4, respectively, i.e., adhering to an effective plate scale of 0.72 Mm and 1.44 Mm, respectively. The binning applied to reduce the resolution of the data uses nearest-neighbor averaging, i.e., by taking the magnetic field data of 2×2 (4×4) neighboring pixels and calculating the mean value.

In order to inspect the effect of binning of the vector magnetic field data (later used as an input for NLFF modeling; see Sect. 2.3), we compute two commonly used area-integrated quantities for each of our target ARs at each spatial resolution, namely the total unsigned magnetic flux, $|\Phi_m|$, defined as

$$|\Phi_m| = \int_{S\,(z=0)} |B_z| \cdot \mathrm{d}S, \tag{3}$$

with B_z being the vertical component of the vector magnetic field data, as well as the unsigned vertical current, $|I_z|$, defined as

$$|I_z| = \int_{S\,(z=0)} |J_z| \cdot \mathrm{d}S, \tag{4}$$

where J_z is the vertical current density and $\mu_0 J_z = (\nabla \times \boldsymbol{B})_{z=0}$.

For the bin[2,4]-based estimates we compute average changes across the time series of the individual ARs with respect to the respective original-resolution (bin1-data) based estimates as

$$\delta\xi_{\mathrm{bin}X} = \frac{1}{n_t} \sum_{i=1}^{n_t} \frac{\xi_{\mathrm{bin}X}(t_i) - \xi_{\mathrm{bin}1}(t_i)}{10^{-2}\xi_{\mathrm{bin}1}(t_i)} \tag{5}$$

where $X = [2, 4]$ for the bin[2,4]-based modeling and n_t is the total number of time instances, $n_t = \sum t_i$.

The HMI data at successively lower spatial resolutions exhibits successively lesser unsigned fluxes and current. This is actually expected because the binning necessarily reduces the strength of and gradients within the original magnetic field data. From application of Eq. (5) to the time series of unsigned fluxes we find $\delta|\Phi_m|\simeq[-1.3\pm0.1,-3.6\pm0.1]\%$ for the bin[2,4] vector magnetic field data of AR 11158 (Fig. 1(a)), of $[-2.4\pm0.0,-5.5\pm0.1]\%$ for AR 11429 (Fig. 1(b)), and of $[-1.9\pm0.1,-4.8\pm0.2]\%$ for AR 12673 (Fig. 1(c)).

For the unsigned vertical current we find $\delta|I_z|\simeq[-42.8\pm0.4,-68.6\pm0.4]\%$ for AR 11158,
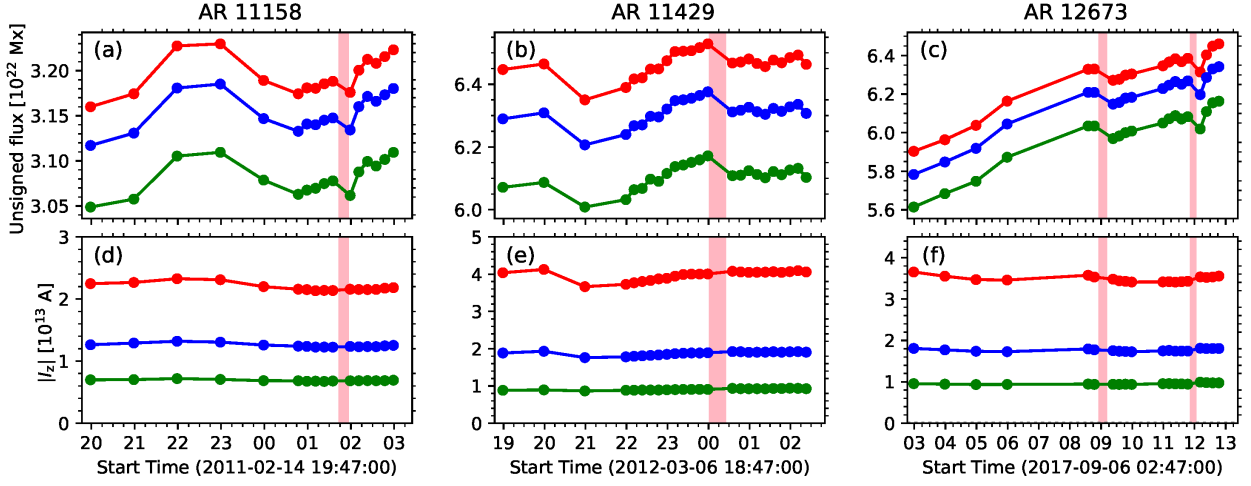
Fig. 1. Area-integrated parameters computed from the photospheric vector data as a function of time for three ARs, and at three different spatial resolutions. *Top:* Unsigned magnetic flux, $|\Phi_m|$. *Bottom:* Unsigned vertical current, $|I_z|$. Red, blue, and green color correspond to bin1, bin2 and bin4 data, respectively, with inherent plate scales of ∼0.36, ∼0.72, and ∼1.4 Mm. Vertical bars indicate the impulsive phase of X-class flares that occurred during the analyzed time intervals.

$[-52.8\pm0.3, -77.1\pm0.4]\%$ for AR 11429, and $[-49.2\pm1.2, -72.6\pm0.9]\%$ for AR 12673 (Fig. 1(d)–(f), respectively). This is in line with the successively lesser electric current found from lower-resolution data in DeRosa et al. (2015). Based on binned SOT-SP spectra, relative changes of the mean vertical current density of $[-43.8, -68,6]\%$ can be deduced for spatial scales corresponding to those used in our study. To compute those percentages, we first defined a reference level from their "bin3" and "bin4" cases, corresponding to an approximate plate scale of ∼0.37 Mm, i.e., comparable to the plate scale our bin1 case. The corresponding estimates of $\langle J_z \rangle$ (cf. their Fig. 4c) were then used to compute a corresponding average value of $\langle [J_{z,bin3}, J_{z,bin4}] \rangle \simeq 12$ mA m^{-2}. Similarly, we compute $\langle [J_{z,bin6}, J_{z,bin8}] \rangle \simeq 6.8$ mA m^{-2} for an approximate plate scale of ∼0.74 Mm, i.e., comparable to our bin2 case, and use their their $J_{z,bin14}$ at a plate scale of ∼1.48 Mm as comparable to our bin4 case.

2.3. Magnetic field modeling

We employ NLFF models from the data time series at the three different plate scales (∼0.36, ∼0.72, and ∼1.4 Mm) for each of the three target ARs. We use the method of Wiegelmann et al. (2012), which involves two main computational steps, a preprocessing of the 2D input data (to retrieve a force-free consistent boundary condition at $z = 0$ Wiegelmann et al. 2006) and subsequent extrapolation (allowing deviations from the input data at $z = 0$ in order to account for measurement uncertainties Wiegelmann & Inhester 2010). During both of those steps, larger freedom is given to changes of the horizontal than to the vertical magnetic field components, in accordance to the generally lower measurement accuracy of the former and higher accuracy of the latter. For completeness we note here that the trend of higher-resolution data hosting more unsigned flux and stronger vertical currents is preserved during preprocessing as well as during optimization. In contrast to Gupta et al. (2021), we employ only one time series per target AR and spatial resolution using standard model parameter settings. In other words, we omit to tune model parameters in order to improve the NLFF model results (for dedicated in-depth studies see, e.g., Thalmann et al. 2019, 2020). This is because we want to obtain insights onto the effects

purely due to the different spatial resolution of the (input) data used for NLFF modeling and to avoid complicating the (already complex) interpretation of dependencies. Thus, we compute 195 NLFF models in total (at three different spatial resolutions for the considered number of time instance listed in the last column in Table 1).

From each modeled NLFF solution for $\boldsymbol{B}$, we compute the unsigned magnetic flux and unsigned vertical current using Eqs. (3) and (4), respectively, at the NLFF models' lower boundary ($z = 0$). In addition, we compute the total (volume-integrated) magnetic energy, E, as,

$$E = \int_V |\boldsymbol{B}|^2 \, dV. \tag{6}$$

Correspondingly, we compute the potential energy, E_0, by using the current-free (minimum-energy) magnetic field solution, $\boldsymbol{B}_0$, in Eq. (6). The latter is defined as $\boldsymbol{B}_0 = \nabla\phi$, with ϕ being the scalar potential, subject to the constraint $\nabla_n \phi = B_n$ on the volume-bounding surface, ∂V. Then we are also able to compute the free magnetic energy as $E_F = E - E_0$.

2.3.1. Quality measures

For the purpose of quantifying the force-freeness of the obtained NLFF model magnetic fields in three dimensions, we use the current-weighted angle between the modeled magnetic field and the electric current density, θ_J, related to the otherwise often used current-weighted average of the sine of the angle between the current density and the magnetic field, σ_J ("CW sinθ"; Wheatland et al. 2000) by $\langle \theta_J \rangle = \sin^{-1} \sigma_J$. As commonly done, we compute the average angle over all grid points, $\langle \theta_J \rangle$. For a completely force-free field, $\langle \theta_J \rangle = 0$.

In order to determine the degree of solenoidality, we employ several different measures commonly used for such purposes. On the one hand we use the fractional flux as defined in Gilchrist et al. (2020), namely $\langle |f_d| \rangle = (6\,\delta x) \langle |f_i| \rangle$, with δx representing the spacing of the Cartesian mesh and $\langle |f_i| \rangle$ representing volume-average of the magnitude of the fractional flux increase in a small discrete volume about each grid point (Wheatland et al. 2000). Being nearly resolution-invariant, $\langle |f_d| \rangle$

serves as an ideal tool for the comparison of the solenoidal levels of NLFF models at different spatial resolutions while covering the same physical volume.ś

On the other hand, we use measures based on the decomposition of the magnetic energy into solenoidal and non-solenoidal parts, the latter being non-zero if the considered magnetic field is not exactly divergence free. Valori et al. (2013) defined a corresponding measure as E_{div}/E, quantifying the fraction of the total magnetic energy which is related to the non-zero divergence of a tested 3D field B, where $E_{\mathrm{div}} = E_{0,ns} + E_{\mathrm{J},ns} + |E_{\mathrm{mix}}|$. Here, $E_{0,ns}$ and $E_{\mathrm{J},ns}$ are the energies of the non-solenoidal components of the potential and current-carrying ($B_{\mathrm{J}} = B - B_0$) magnetic field, respectively, and E_{mix} is a mixed potential-current carrying term (see Eq. (8) of Valori et al. 2013, for details), the latter usually representing the largest contribution to the non-solenoidal energies (see Sect. 5 in that work and also Sect. 3.1.2 in DeRosa et al. (2015)). Dedicated follow-up studies examined that $E_{\mathrm{div}}/E \simeq 0.1$ (at the most) is to be tolerated when B is used for subsequent computation of magnetic helicity (Valori et al. 2016; Thalmann et al. 2019). In that context, Thalmann et al. (2020) suggested to use an even more restrictive quantity, namely the ratio $|E_{\mathrm{mix}}|/E_{\mathrm{J},s}$ as a criterion to disqualify a given B for subsequent helicity computation, where $E_{\mathrm{J},s}$ is the energy of the solenoidal component of the current-carrying field (equivalent to the free magnetic energy in a perfectly solenoidal field), and suggested a corresponding threshold to be respected as $|E_{\mathrm{mix}}|/E_{\mathrm{J},s} \lesssim 0.4$. Since the purpose of our work is to explore all effects caused by a change of the spatial resolution of the input data, we do check whether or not $E_{\mathrm{div}}/E=0.1$ and/or $|E_{\mathrm{mix}}|/E_{\mathrm{J},s}=0.4$ are exceeded in our NLFF model time series, yet do not exclude them from subsequent helicity computation. In order to identify corresponding time instances we mark them separately in the figures of our Results section 3. This allows us to understand the resolution-induced variations to a reliable helicity computation in that matter.

2.4. Magnetic helicity and its computation

The gauge-invariant relative magnetic helicity in a volume, V, can be written as (Berger & Field 1984; Finn & Antonsen 1984)

$$H_V = \int_V (A + A_0) \cdot (B - B_0) \, dV, \qquad (7)$$

where A and A_0 are the respective vector potentials satisfying $B = \nabla \times A$ and $B_0 = \nabla \times A_0$. H_V in Eq. (7) can be decomposed as, $H_V = H_{\mathrm{J}} + H_{\mathrm{PJ}}$ (Berger 1999, 2003), with

$$H_{\mathrm{J}} = \int_V (A - A_0) \cdot (B - B_0) \, dV, \qquad (8)$$

$$H_{\mathrm{PJ}} = 2 \int_V A_0 \cdot (B - B_0) \, dV, \qquad (9)$$

where H_{J} is the magnetic helicity of the current-carrying field, B_{J}, and H_{PJ} is the volume-threading helicity, both being separately gauge invariant (Linan et al. 2018).

We compute the vector potentials A and A_0, required for the computation of the relative helicities in Eqs. (7)–(9), using method of Thalmann et al. (2011). The method solves systems of partial differential equations to obtain the vector potentials A and A_0, using the Coulomb gauge, $\nabla \cdot A = \nabla \cdot A_0 = 0$. The method has been shown to provide solutions of A and A_0 superior regarding their degree of solenoidality and to deliver helicities in line with that of other existing methods (Valori et al. 2016).

3. Results

In the following, we summarize the quality (Sect. 3.1) of the NLFF modeling as well as deduced physical quantities (Sect. 3.2) at different spatial resolutions. To do so, we compute time-series averaged changes with respect to the original-resolution (bin1) model time series, by evaluating Eq. (5) for the analyzed quantities.

3.1. NLFF model quality

The NLFF time series of ARs 11158 and 11429 (Fig. 2(a) and (b), respectively) exhibit values of $\langle\theta_J\rangle \lesssim [10°, 7°, 6°]$ for the bin[1,2,4]-based solutions, implying that the force-free quality is systematically higher at lower spatial resolution. The overall changes computed for the bin[2,4]-based time series are $\delta\langle\theta_J\rangle \simeq [-24.1\pm4.6, -33.4\pm4.7]\%$ for AR 11158 and $\simeq [-32.8\pm4.2, -44.0\pm3.2]\%$ for AR 11429. Thought not shown explicitly, we note that similar findings are obtained from the analysis of $\langle CW \sin\theta\rangle$. The situation is different for AR 12673, for which no such systematic improvement of $\langle\theta_J\rangle$ at successively lower spatial resolutions is observed (Fig. 2(c)). While the bin2-based solutions exhibit comparably lowest values of $\langle\theta_J\rangle$ before the occurrence of the first X-class flare (before ~09:00 UT) it is the bin4-based solutions doing so after its occurrence (between ~09:24 and 10:00 UT; see inlet to Fig. 2(c)).

From the decomposition of the magnetic energy, we find for AR 11158 values of $E_{\mathrm{div}}/E \lesssim [0.04, 0.03, 0.02]$ for the bin[1,2,4]-based NLFF models, respectively (Fig. 2(d)), i.e., the solutions at lower spatial resolution are of higher solenoidal quality. Similarly, we find values of $E_{\mathrm{div}}/E \lesssim [0.13, 0.09, 0.06]$ for the bin[1,2,4]-based NLFF models for AR 11429 (Fig. 2(e)). More precisely, the overall changes across the bin[2,4]-based time series, with respect to the corresponding bin1-based time series, are $\delta E_{\mathrm{div}}/E \simeq [-40.6\pm3.4, -58.3\pm7.5]\%$ for AR 11158 and $\simeq [-38.8\pm3.0, -57.2\pm1.5]\%$ for AR 11429, i.e., a comparable overall improvement of solenoidal quality at successively lower spatial resolution is observed for the two ARs. This is different for AR 12673 where the bin2-based series appears as to be of highest solenoidal quality, followed by the bin1- and bin4-bases series (Fig. 2(f)), suggesting E_{div}/E not to scale with underlying spatial resolution.

Note also that $E_{\mathrm{div}} = 0.1$ is occasionally exceeded within the individual time series, i.e., specific solutions may not be suited for trustworthy subsequent computation of magnetic helicity (see Sect. 2.3.1 for details). For instance, the bin1-based NLFF models of AR 11429 prior to the occurrence of the X-class flare exhibit values of $E_{\mathrm{div}}/E > 0.1$ (see horizontal line in Fig. 2(e) for reference). For AR 12673 the situation is even more dramatic, where the NLFF models at all three spatial resolutions exhibit values of $E_{\mathrm{div}}/E > 0.1$ at various time instances after the occurrence of the first X-class flare (after ~09:12 UT; see inlet to Fig. 2(f)).

For the ratio, $|E_{\mathrm{mix}}|/E_{\mathrm{J},s}$, we find values of $\lesssim [0.15, 0.10, 0.06]$ for the bin[1,2,4]-based NLFF models of AR 11158 (Fig. 2(g)), and in the range $\lesssim [0.30, 0.20, 0.15]$, for AR 11429 (Fig. 2(h)). That corresponds to overall changes across the bin[2,4]-based time series of $\delta |E_{\mathrm{mix}}|/E_{\mathrm{J},s} \simeq [-42.2\pm3.3, -66.2\pm7.5]\%$ for AR 11158 and $\simeq [-37.3\pm3.9, -57.9\pm2.3]\%$ for AR 11429. Thus, as before for E_{div}/E, a comparable overall improvement of solenoidal quality at successively lower spatial resolution is observed for the two ARs. Comparatively larger values of $|E_{\mathrm{mix}}|/E_{\mathrm{J},s} \lesssim 0.4$ are found for AR 12673 prior to the occurrence of the first X-class flare, while increasing to larger values after
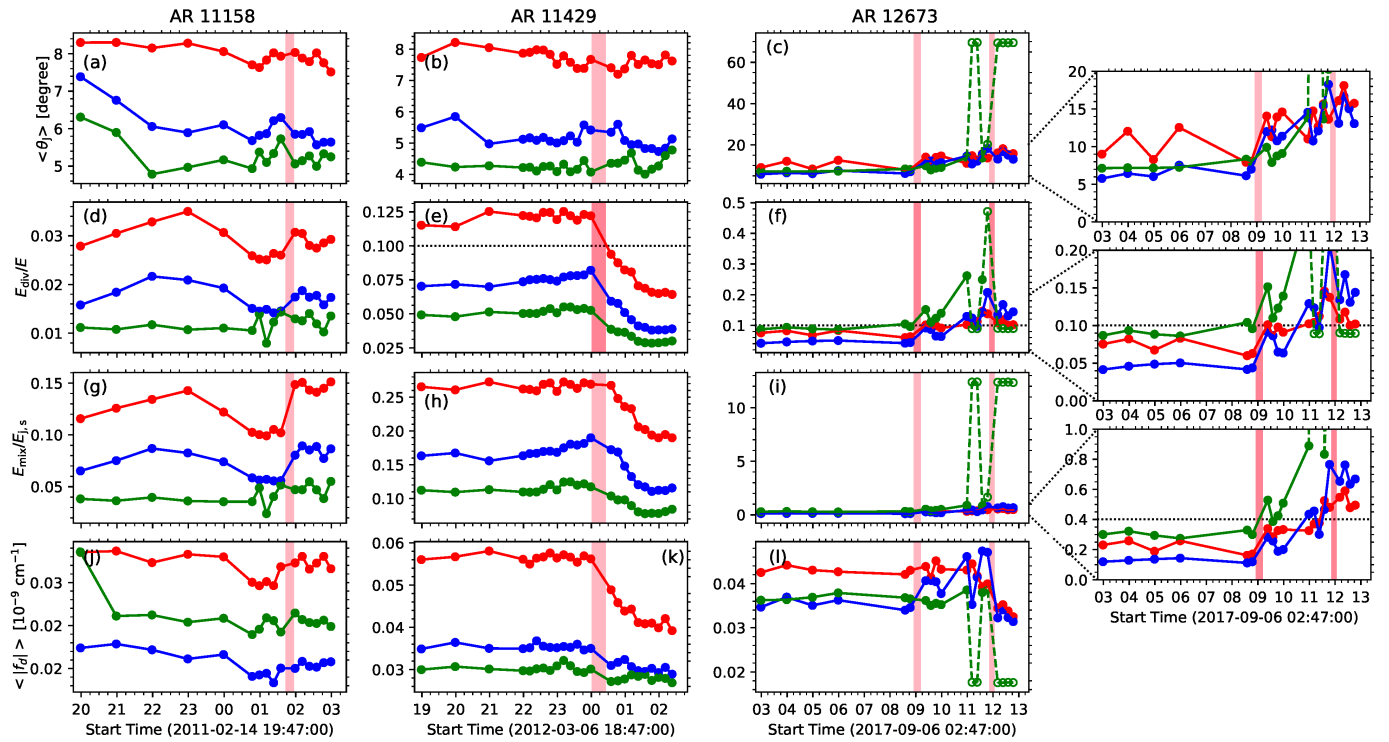
Fig. 2. Quality of the NLFF solutions. From top to bottom for the individual ARs are shown: the volume-averaged current-weighted angle, $\langle\theta_J\rangle$, the fraction of non-solenoidal to total magnetic energy, $E_{\rm div}/E$, the ratio $|E_{\rm mix}|/E_{J,s}$, and its resolution-invariant complement, $\langle|f_d|\rangle$. Red, blue, and green color correspond to bin1, bin2 and bin4 data, respectively, with inherent plate scales of ~0.36, ~0.72, and ~1.4 Mm. Empty symbols mark disqualifying NLFF solutions (see Sect. 3.1 for explanation). The inlets in the rightmost column show a subrange of values for enhanced visibility. Vertical bars indicate the impulsive phase of X-class flares that occurred during the analyzed time intervals.

the occurrence of the second X-class flare (see inlet to Fig. 2(i)). Notably, extreme values of $|E_{\rm mix}|/E_{J,s}>1$ are found from the bin4-bases solutions. It will be shown in Sect. 3.2.2 that those models exhibit a negative free energy budget (hence are to be dubbed "non-physical") and are observed in conjunction with low force-free quality ($\langle\theta_J\rangle\gtrsim20°$; compare Fig. 2(c)), indicating the very failure of successful extrapolation.

The computed values of the fractional flux are in the range $\langle|f_d|\rangle(\times10^9\,{\rm cm}^{-1})\lesssim[0.04,0.02,0.03]$ for the bin[1,2,4]-based NLFF models of AR 11158 (Fig. 2(j)), $\lesssim[0.06,0.04,0.03]$ for AR 11429 (Fig. 2(k)), and $\lesssim[0.05,0.05,0.04]$ for AR 12673 (Fig. 2(l)). In other words, while for AR 11158 the bin2-based modeling exhibits lowest values of $\langle|f_d|\rangle$, it is the bin4-based modeling for AR 11429, quite consistently across the corresponding time series. For AR 12673, again, NLFF models qualitatively superior at distinct time instance are not necessarily associated to a systematically different spatial resolution. In fact, higher/lower values of $\langle|f_d|\rangle$ tend to be found together with larger/smaller values of $\langle\theta_J\rangle$ (compare Fig. 2(c)). The problematic bin4-based solutions of AR 12673 (for which also extreme values of $\langle\theta_J\rangle$ and $|E_{\rm mix}|/E_{J,s}$ and partly $E_{\rm div}/E$ were found) exhibit lowest values ($\langle|f_d|\rangle\lesssim0.02$; see symbols marked by empty circles in Fig. 2(l)), i.e., suggest a high solenoidal quality on the contrary.

3.2. NLFF-model deduced quantities

In the following, we analyze physical quantities deduced from the NLFF model time series at different spatial resolutions. As above, we do so by evaluating time-series averaged changes computed from Eq. (5), albeit disregarding non-physical solu-

tions ($E_{\rm F}<0$) within the individual time series (marked by empty plot symbols in Figs. 3 and 4). In addition, when analyzing the magnetic helicity in Sect. 3.2.3 we also disregard NLFF solutions with non-negligible solenoidal errors ($E_{\rm div}/E>0.1$; marked by empty plot symbols in Figs. 5).

3.2.1. Unsigned flux and current

From the bin[2,4]-based NLFF model lower boundaries, using the bin1-based time series as the base against which to compute the percentage changes, we find for AR 11158 $\delta|\Phi_m|\simeq[-3.6\pm0.3,-8.5\pm0.4]\%$ (Fig. 3(a)). For AR 11429, the corresponding changes are $\delta|\Phi_m|\simeq[-4.7\pm0.8,-11.0\pm1.1]\%$ (Fig. 3(b)) and for AR 12673 they are $\delta|\Phi_m|\simeq[-3.5\pm1.2,-10.8\pm1.0]\%$ (Fig. 3(c)). Furthermore, for AR 11158 we find $\delta|I_z|\simeq[-31.8\pm2.6,-47.1\pm2.1]\%$ (Fig. 3(d)), $\simeq[-26.4\pm4.7,-43.7\pm3.6]\%$ for AR 11429 (Fig. 3(e)), and $\simeq[-17.6\pm14.8,-43.7\pm10.1]\%$ for AR 12673 (Fig. 3(f)).

Note that the final NLFF model lower boundary data necessarily differs from the input data (cf. Sect. 2.2) since they are altered once during the preprocessing step and also iteratively updated during the optimization process (for details see Sect. 2.3). As a consequence, $|\Phi_m|$ computed from NLFF model lower boundaries is lower than in the corresponding input data (up to $\approx10\%$ at most), as is $|I_z|$ (up to $\approx40\%$ at most). Changes to the input data, especially to the horizontal magnetic field components are expected due to their inconsistency with the force-free assumption. Also, they are known to be substantial in comparison to the uncertainties of the input data (for a corresponding analysis see, e.g., Sect. 3.2 of DeRosa et al. 2015). Qualitatively, however, the trends within the individual NLFF lower boundary-
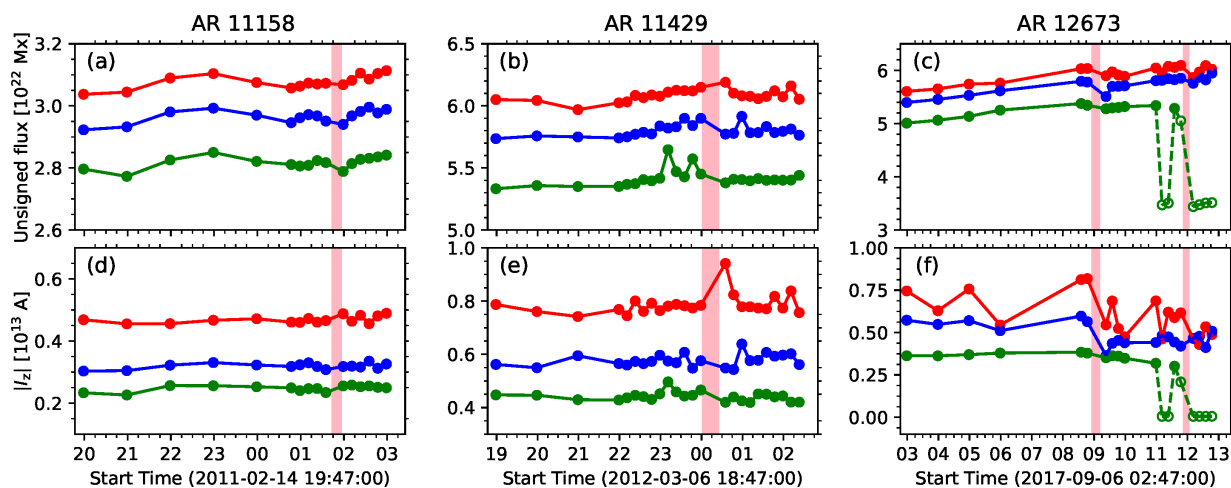
Fig. 3. Area-integrated parameters computed from the NLFF lower boundary data as a function of time for three ARs, and at three different spatial resolutions. *Top:* Unsigned magnetic flux, $|\Phi_m|$. *Bottom:* Unsigned vertical current, $|I_z|$. Red, blue, and green color correspond to bin1, bin2 and bin4 data, respectively, with inherent plate scales of ~0.36, ~0.72, and ~1.4 Mm. Vertical bars indicate the impulsive phase of X-class flares that occurred during the analyzed time intervals.

based time series are similar to those in the corresponding input data time series (with the exception of those which stem from unphysical NLFF solutions) and the induced changes are on the order of the resolution-induced changes as listed earlier.

3.2.2. Magnetic energy

For all three considered ARs, the computed potential field energies, E_0, are smaller at reduced spatial resolution (Fig. 4(a)–(c)). More quantitatively, in comparison to E_0 from the corresponding bin1-based NLFF model time series, changes are found as $\delta E_0 \simeq [-0.6\pm0.2, -4.0\pm0.5]\%$ for AR 11158, $\simeq [-0.4\pm0.1, -2.1\pm0.5]\%$ for AR 11429, and $\simeq [-0.9\pm0.8, -5.6\pm0.7]\%$ for AR 12673, for the bin[2,4]-based time series, respectively.

On overall larger values of total magnetic energies, E, are found at lower spatial resolution for ARs 11158 and 11429 (Fig. 4(d) and (e), respectively). More quantitatively, in comparison to the bin1-data based NLFF models, changes of $\delta E \simeq [1.4\pm0.4, 2.3\pm1.3]\%$ for AR 11158, $\simeq [3.7\pm0.8, 7.4\pm0.8]\%$ for AR 11429, at bin[2,4], respectively. In contrast, and similar to all other analyzed quantities so far, no such systematic dependence of E on underlying spatial resolution is found for AR 12673 (Fig. 4(f)). Here, we find $\delta E \simeq 1.3\pm5.0\%$ for the bin2-based and $\delta E \simeq -11.5\pm4.1\%$ for the bin4-based NLFF model time series.

For the free magnetic energies, E_F, trends similar to that of the corresponding values of E are noticed (see Fig. 4(g)–(i)). More quantitatively, on overall and in comparison to the bin1-data based NLFF models the bin[2,4]-based estimates are found as $\delta E_F \simeq [10.2\pm2.7, 29.8\pm10.0]\%$ for AR 11158 and $\simeq [13.9\pm2.9, 31.2\pm4.7]\%$ for AR 11429. In contrast, we find $\simeq [6.3\pm29.4, -32.7\pm18.6]\%$ for AR 12673 (Fig. 4(i)). The non-physical solutions, such as the bin4-based NLFF models of AR 12673 at the end of the considered time interval where $E_F < 0$ (see empty plot symbols in Fig. 4(i)) have been identified earlier already based on outstandingly poor NLFF model quality metrics (see Sect. 3.1 for details) and were not considered for computation of the percentages above.

We note that the spatial resolution-induced changes to E_0 reflect those observed for $|\Phi_m|$. That may be expected as the po-

tential field is determined from the vertical field on the model volume's lower boundary. In contrast. E and E_F show a different behavior than the supposedly indicative unsigned vertical current ($|I_z|$). Naively one would expect to find larger corresponding values for larger values of $|I_z|$, as the latter represents a measure of enhanced complexity in the horizontal field. Though it is true that a higher spatial resolution on overall relates to higher values of $|I_z|$ (cf. Fig. 3), this is not true for E. Consequently, this is also not true for the free magnetic energy (compare Fig. 4(d)–(i)) as it is calculated as $E_F = E - E_0$, and E_0 is larger at higher spatial resolutions. For completeness, we note here that we also inspected the volume-integrated total unsigned current, $|I_{tot}|$, in order to better understand the obtained total energies. Though not shown explicitly, trends throughout the individual time series as well as resolution-induced changes are found very similar to to that of E and E_F, i.e., larger integrated values at lower spatial resolutions.

This apparent discrepancy can partly be resolved by comparison to the solenoidal quality of the NLFF models in Fig 2, revealing a rather obvious dependency. Both, trends within the individual time series (at different spatial resolutions) as well as resolution-induced changes for time series of individual ARs are found to be reflected 1:1 in the time series of $|E_{mix}|/E_{J,s}$ (and to a somewhat lesser extent on E_{div}/E in conjunction with $\langle\theta_J\rangle$). More precisely, volume-integrated energies (and unsigned currents) are higher for NLFF models of higher the solenoidal quality. For instance, the bin4-based NLFF models of ARs 11158 and 11429 exhibit larger values of E, E_F (and $|I_{tot}|$) in conjunction with lowest values of $|E_{mix}|/E_{J,s}$ than at other spatial resolutions. In contrast the bin4-based NLFF models of AR 12673 exhibit lower energies than at other spatial resolutions (bin1 and bin2) and simultaneously exhibit larger values of $|E_{mix}|/E_{J,s}$.

3.2.3. Magnetic helicity

For the total relative helicity, H_V, on overall and in comparison to the bin1-data based NLFF models the bin[2,4]-based estimates changes are found as $\delta H_V \simeq [-17.9\pm5.6, -40.7\pm9.9]\%$ for AR 11158 and $\simeq [-1.6\pm0.7, -0.7\pm1.0]\%$ for AR 11429 (Fig. 5(a) and (d), respectively). Similarly, one finds $\delta H_{PJ} \simeq [-23.7\pm6.3, -52.4\pm12.7]\%$ for AR 11158 and $\simeq [-4.1\pm0.8, -5.9\pm1.2]\%$ for AR 11429, respectively (Fig. 5(b)
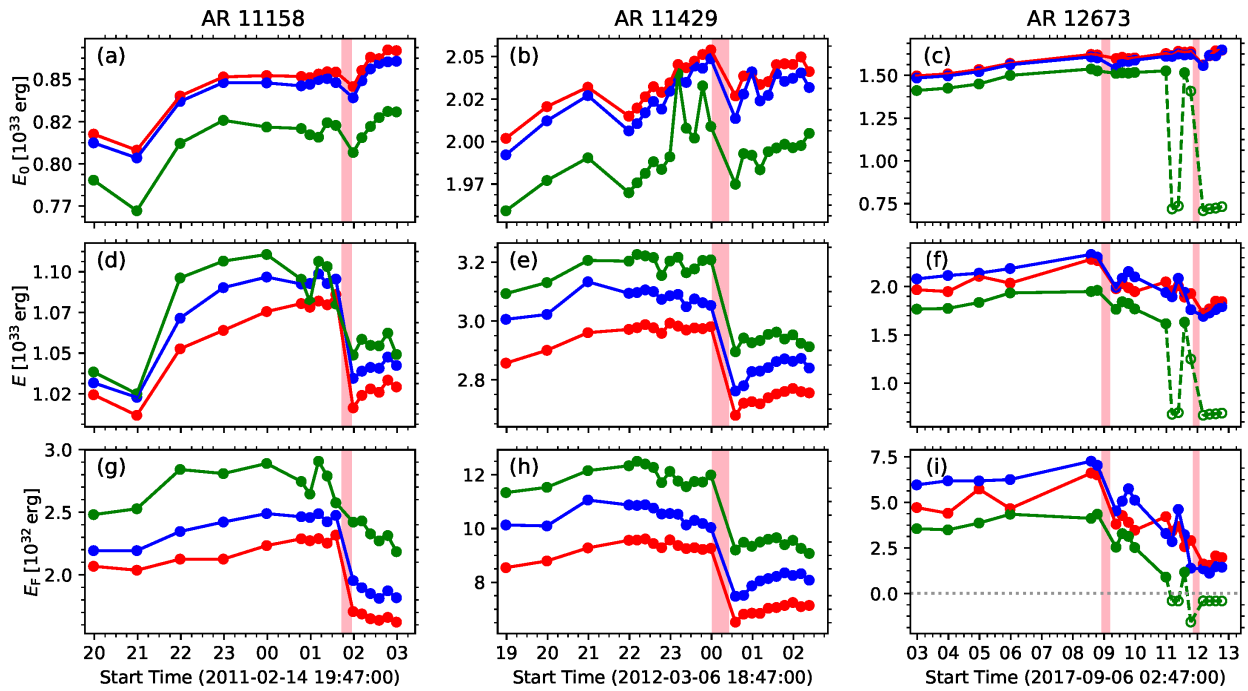
Fig. 4. Volume-integrated magnetic energies computed from the NLFF solutions as a function of time for three ARs, and at three different spatial resolutions. *Top:* Potential energy, E_0. *Middle:* Total energy, E. *Bottom:* Free magnetic energy, $E_F = E - E_0$. Red, blue, and green color correspond to bin1, bin2 and bin4 data, respectively, with inherent plate scales of $\sim$0.36, $\sim$0.72, and $\sim$1.4 Mm. Vertical bars indicate the impulsive phase of X-class flares that occurred during the analyzed time intervals.

and (e), respectively). In contrast, comparatively lower values of the current-carrying helicities, H_J, are found at higher spatial resolutions (Fig. 5(g) and (h), respectively), with $\delta H_J \simeq [16.5 \pm 6.7, 31.7 \pm 15.8]\%$ and $\simeq [17.9 \pm 2.6, 39.5 \pm 7.2]\%$, respectively. In contrast, and similar to all other quantities analyzed for AR 12673 so far, no apparent dependencies of the relative helicities on the underlying spatial resolution there. Instead, $\delta H_V \simeq [9.8 \pm 5.2, -22.6 \pm 3.8]\%$ (Fig. 5(c)), $\delta H_{PJ} \simeq [6.2 \pm 4.0, -22.4 \pm 2.9]\%$ (Fig. 5(f)), and $\delta H_J \simeq [48.5 \pm 24.4, -24.0 \pm 12.8]\%$ (Fig. 5(i)) for the bin[2,4]-based modeling, respectively.

Again, the comparison to the solenoidal quality of the underlying NLFF models (Fig. 2) reveals a dependency of the relative helicities, very similar to that found for the magnetic energies (Sect. 3.2.2). This can be seen from the bin4-based NLFF models of AR 12673, which yield lower values for the relative helicities and simultaneously larger values of $|E_{mix}|/E_{J,s}$ than the corresponding models at higher spatial resolutions (bin2 and bin1).

4. Discussion

We demonstrated that the resolution-induced effects are not only different at different times (for a specific AR) but also distinctly different for different ARs. The chosen setup in this study (the employing of three NLFF time series at different spatial resolutions for three different ARs) furthermore allows us to study overall trends to be expected for NLFF modeling (and subsequent magnetic energy and helicity computations). Therefore, we calculate histograms of the changes to the physical variables due to a reduction of the spatial resolution, i.e., we compute the differences between all qualifying bin2- and bin4-based NLFF solutions, if a corresponding bin1-based NLFF model qualifies for comparison (i.e., suffices the same quality criteria). Generally, a NLFF model qualifies if it is physical ($E_F > 0$; 59

NLFF models at bin2 and 52 at bin4). It qualifies for subsequent helicity-computation if it is sufficiently solenoidal ($E_{div}/E \leq 0.1$; 35 NLFF models at bin2 and 31 at bin4). For those, median values as well as corresponding median absolute deviations for the induced changes (denoted by angular brackets hereafter) are discussed in the following, and interpreted in context with the changes to the individual NLFF model time series listed in Sect. 3.

A first main finding of our analysis regards the relative power of distinct metrics to measure the quality of NLFF models. When using the most indicative (sensitive) metrics for a corresponding quantification, we find that on overall the NLFF model quality is higher at reduced spatial resolutions. Using $\langle \theta_J \rangle$ as a measure, median changes by $\langle \delta \langle \theta_J \rangle \rangle \approx -26.4 \pm 3.8\%$ and $\approx -34.3 \pm 5.2\%$ are found for the bin2-based and bin4-based modeling, respectively (Fig. 6(a)), using the bin1-based NLFF modeling as a reference (which is used as a basis for all median changes listed in the following). Though not explicitly shown, we note that the corresponding analysis of $\langle CW \sin\theta \rangle$ allows a very similar statement. An improvement of the solenoidal quality of the NLFF models at lower spatial resolution might be expected, as the application of binning to mimic the reduction of spatial resolution reduces gradients present in the original data, i.e., should yield a reduction of $\nabla \cdot \mathbf{B}$. Corresponding conclusions can be drawn from the quantities most sensitive to the solenoidal quality of a magnetic field, E_{div}/E and $|E_{mix}|/E_{J,s}$. Here, median changes are found as $\langle \delta E_{div}/E \rangle \approx [-37.8 \pm 3.7, -43.7 \pm 6.1]\%$ for the bin[2,4]-based modeling (Fig. 6(b)) and $\langle \delta |E_{mix}|/E_{J,s} \rangle \approx [-39.7 \pm 3.0, -45.9 \pm 7.2]\%$, respectively (Fig. 6(c)). Those two measures were found most sensitive (and indicative) regarding the solenoidal quality of the tested NLFF models in Sect. 3.1 (see also Thalmann et al. 2019), superior to the use of an alternative metrics to quantify the divergence-freeness, such as $\langle |f_i| \rangle$ and $\langle |f_d| \rangle$.
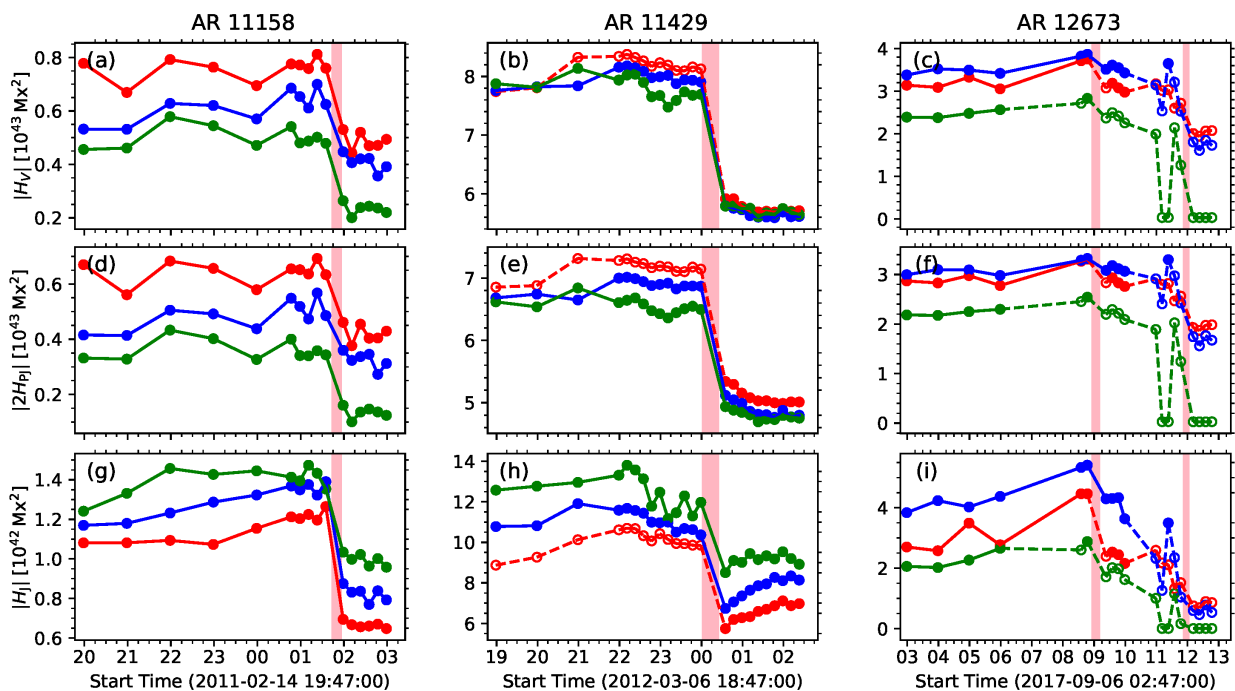
Fig. 5. Volume-integrated relative helicities computed from the NLFF solutions as a function of time for three ARs, and at three different spatial resolutions. *Top:* Total helicity, H_V. *Middle:* Volume-threading helicity, H_{PJ}. *Bottom:* Helicity of the current-carrying field, H_J. Red, blue, and green color correspond to bin1, bin2 and bin4 data, respectively, with inherent plate scales of ~0.36, ~0.72, and ~1.4 Mm. Vertical bars indicate the impulsive phase of X-class flares that occurred during the analyzed time intervals.

DeRosa et al. (2015) used $\langle|f_i|\rangle$ as a measure to quantify the divergence-free quality at different spatial resolutions, according to which the analyzed optimization-based modeling exhibited successively larger values at lower spatial resolutions (see their Table 2). In fact, if were to draw conclusions based on $\langle|f_i|\rangle$, we would judge based on corresponding median values of $\langle\langle|f_i|\rangle \times 10^4\rangle \approx [2.5\pm0.5, 3.7\pm0.4, 6.9\pm0.5]$ for bin[1,2,4]-based modeling, respectively, we would arrive at a similar conclusion as DeRosa et al. (2015), namely that the divergence-free property is improved at increased spatial resolution. Yet, $\langle|f_i|\rangle$ has recently been dubbed inappropriate for the purpose of analyzing resolution-induced aspects by Gilchrist et al. (2020), who proposed an improved (refined) corresponding measure, $\langle|f_d|\rangle$, nearly insensitive to the spatial resolution of the analyzed NLFF solution. Here, we find median values of $\langle\langle|f_d|\rangle \times 10^{11} cm^{-1}\rangle \approx [4.2\pm0.9, 3.1\pm0.3, 3.0\pm0.3]$ for bin[1,2,4]-based modeling, respectively, i.e., lowest divergence-freeness at highest spatial resolution. In fact, the trend of a lower solenoidal quality at higher spatial resolution can also be deduced from the optimization-based NLFF models studied in DeRosa et al. (2015) (see their Table 4), we can obtain average estimates for plate scales that correspond approximately to those used in our study ([0.36, 0.72, 1.44] Mm for our bin[1,2,4] cases, respectively). In particular, we compute $\langle[(E_{div}/E)_{bin6}, (E_{div}/E)_{bin8}]\rangle \approx 0.08$ (corresponding to an average plate scale of ~0.74 Mm) and use their $(E_{div}/E)_{bin14} = 0.06$ (corresponding to an average plate scale of ~1.48 Mm), to find a solenoidal quality improved by ≈12% and ≈33%, respectively, with respect to their $\langle[(E_{div}/E)_{bin3}, (E_{div}/E)_{bin4}]\rangle \approx 0.09$ (corresponding to an average plate scale of ~0.37 Mm). Doing the same for $|E_{mix}|/E_{J,s}$, i.e. using $(|E_{mix}|/E_{J,s})_{bin14} \approx 1.00$ and $\langle[(|E_{mix}|/E_{J,s})_{bin6}, (|E_{mix}|/E_{J,s})_{bin8}]\rangle \approx 1.17$, one finds improvements of ≈3% and ≈17%, respectively, with respect to their $\langle[(|E_{mix}|/E_{J,s})_{bin3}, (|E_{mix}|/E_{J,s})_{bin4}]\rangle \approx 1.20$.

As a second major finding, we may state that there are certain overall tendencies regarding how a change of the spatial resolution does translate into a corresponding variation in the deduced physical quantities. On overall, the NLFF lower boundary area-integrated quantities, $|\Phi_m|$ and $|I_z|$, exhibit resolution-dependent variations in the form of a successive reduction when the resolution is reduced (see Sect. 3.2.1 and Fig. 3). This is actually expected because the binning, used to mimic a reduction of the spatial resolution of the data, necessarily reduces amplitudes and gradients with respect to that of the original-resolution data. Though not shown explicitly, we deduce median changes of $\langle\delta|\Phi_m|\rangle \approx [-3.9\pm0.4, -9.6\pm0.9]\%$ for the bin[2,4]-based lower boundary data, and $\langle\delta|I_z|\rangle \approx [-27.3\pm4.7, -46.4\pm2.4]\%$, respectively. The comparatively larger modifications to $|I_z|$ (compared to that of $|\Phi_m|$) are expected, since during NLFF modeling the horizontal magnetic field components are altered to a much larger degree than is the vertical magnetic field component (hence is $|\Phi_m|$; see Sect. 3.2.1 for details).

Intuitively, one would assume to find, corresponding to the lower values of $|\Phi_m|$ and $|I_z|$, also smaller values for the volume-integrated estimates (magnetic energies, electric currents, and magnetic helicities) at successively lower spatial resolutions. That is, however, only partially true. For instance the resolution-induced changes to E_0 are consistent with those found for $|\Phi_m|$, namely $\langle\delta E_0\rangle \approx [-0.6\pm0.2, -3.7\pm1.0]\%$ for bin[2,4]-based NLFF modeling, respectively (Fig. 7(a)). This is also true for the total helicity, with $\langle\delta|H_V|\rangle \approx [-5.9\pm13.2, -25.6\pm14.4]\%$ (Fig. 7(d)), the volume-threading helicity with $\langle\delta H_{PJ}\rangle \approx [-10.3\pm13.1, -33.5\pm19.4]\%$ (Fig. 7(e)), and is also consistent with the corresponding trends seen in $\langle\delta|I_z|\rangle$. In contrast, lesser electric currents do not necessarily translate to systematically lower volume-integrated total energies (Fig. 7(b)), free magnetic energies (Fig. 7(c)), and current-carrying helicities (Fig. 7(f)), for
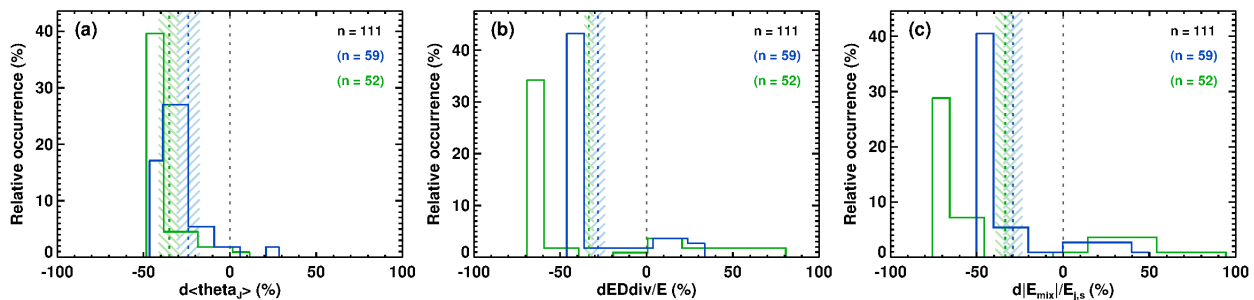
Fig. 6. Histograms displaying the variations of the NLFF model quality, as quantified by (a) $\langle\theta_J\rangle$, (b) E_{div}/E, and (c) $|E_{\mathrm{mix}}|/E_{J,s}$. Relative differences of the bin2- (blue) and bin4- (green) based modeling, with respect to the bin1-based estimates are shown. The total number of considered (qualifying) NLFF models is indicated in black and used as the basis to compute percentages. The total number of qualifying solutions at bin2 and bin4 are indicated in blue and green color, respectively. Median values and median absolute deviation derived from the histograms are shown as dashed vertical lines and shaded bars, respectively.
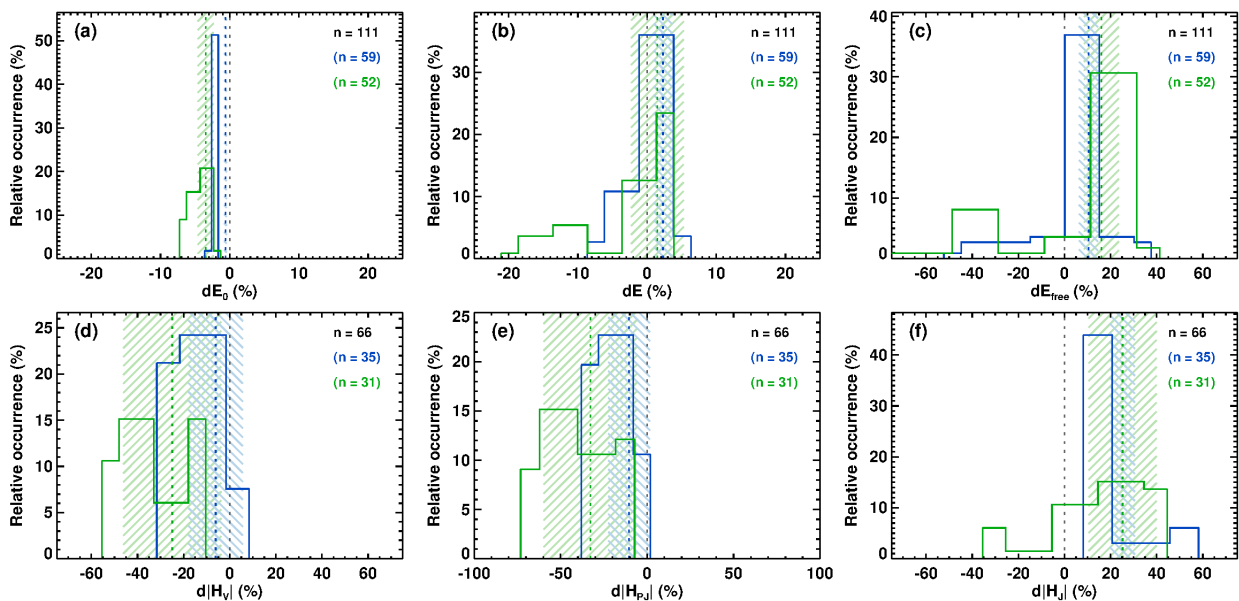

Fig. 7. Histograms displaying the variations of the volume-integrated magnetic energies E_0 (a), E (b), and E_F (c) and absolute relative helicities, H_V (d), H_{PJ} (e), and H_J (f). Relative differences of the bin2- (blue) and bin4- (green) based modeling, with respect to the bin1-based estimates are shown. The total number of considered (qualifying) NLFF models is indicated in black and used as the basis to compute percentages. The total number of qualifying solutions at bin2 and bin4 are indicated in blue and green color, respectively. Median values and median absolute deviation derived from the histograms are shown as dashed vertical lines and shaded bars, respectively.

which successively larger median values are found, namely $\langle\delta E\rangle\approx[3.0\pm1.0,1.6\pm3.3]\%$, $\langle\delta E_F\rangle\approx[16.0\pm4.2,22.0\pm8.1]\%$, and $\langle\delta H_J\rangle\approx[25.6\pm6.3,24.0\pm15.7]\%$ for bin[2,4]-based modeling, respectively.

Thalmann et al. (2013), based on the binning of *Hinode*/SOT-SP data to a plate scale of ~0.5 arcsec (called "SP$_{\mathrm{bin}}$" case in their study and intended to match the spatial resolution of HMI data in their study) reported a binning-induced decrease of the total unsigned flux and potential field energy, along with an increase in total and free magnetic energy, when compared to the NLFF modeling using original-resolution (~0.3 arcsec at disk center; called "SP$_{\mathrm{orig}}$" case in their study) SOT-SP data. In contrast, the optimization-based models based on lower-resolution SOT-SP data in DeRosa et al. (2015) were associated to lesser total and free magnetic energies. As already noted by DeRosa et al. (2015), however, estimates of physical quantities become questionable in the presence of significant residual errors in the divergence of **B**. Now, having the dedicated studies by Valori et al. (2016);

Thalmann et al. (2019, 2020) at hand, optimization-based NLFF solutions may only be trustworthy if they exhibit values of $E_{\mathrm{div}}/E\lesssim0.1$ and $|E_{\mathrm{mix}}|/E_{J,s}\lesssim0.4$. In fact, however, all of the optimization-based models analyzed in the work of DeRosa et al. (2015) exhibited values of $E_{\mathrm{div}}/E\gtrsim0.06$ and $|E_{\mathrm{mix}}|/E_{J,s}\gtrsim0.9$. Measures of the quality of the analyzed NLFF models have not been reported by Thalmann et al. (2013), and due to not knowing better at that time, also not interpreted in context with the obtained estimates of physical parameters. The quality measures for SP-orig model read $E_{\mathrm{div}}/E=0.08$, and $|E_{\mathrm{mix}}|/E_{J,s}=0.55$. For the SP$_{\mathrm{bin}}$ model they read $E_{\mathrm{div}}/E=0.09$, and $|E_{\mathrm{mix}}|/E_{J,s}=0.51$. Thus, observed (apparently resolution-dependent) trends of deduced model-based physical parameters in Thalmann et al. (2013) and DeRosa et al. (2015) must be questioned due to the poor model quality of the underlying NLFF solutions. That makes it difficult to interpret the findings of those studies with respect to those found by our extended approach and NLFF models of high solenoidal quality $\langle E_{\mathrm{div}}/E\rangle\approx[0.05\pm0.03,0.05\pm0.03,0.04\pm0.02]$ and
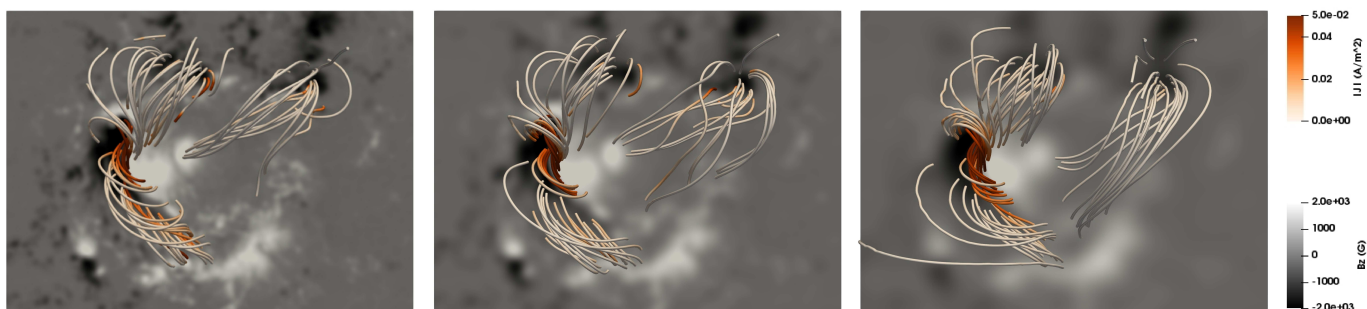
Fig. 8. Morphology of the reconstructed magnetic field of AR 12673 at 08:48 on 6 September 2017 at different spatial resolutions. From left to right, the bin1-, bin2-, and bin4-based modeling is shown. The same footpoints were used in all cases. Field lines are colored according to the magnitude of the electric current density, $|J|$. The gray-scale background resembles B_z of the NLFF lower boundary, scaled to ± 2 kG.

$\langle |E_{\rm mix}|/E_{{\rm J},s}\rangle \approx [0.18\pm0.05, 0.14\pm0.04, 0.11\pm0.03]$ for bin[1,2,4]-based modeling, namely that, generally, binning-induced effects include decreases of unsigned magnetic fluxes and potential field energies, along with increases in total and free magnetic energies.

Besides having figured that the solenoidal quality of NLFF solutions directly affects the resulting volume-integrated estimates, the generally lower model quality of NLFF solutions at higher spatial resolution (Fig. 6) together with the lower values of volume-integrated quantities directly associated to the presence of electric currents (E, $E_{\rm F}$ and $H_{\rm J}$; Fig. 7) raises the question of whether one should favor to employ optimization-based NLFF modeling at a reduced spatial resolution. While this could be validly suggested for applications to HMI data based on the analysis presented here, a general recommendation in that sense cannot be given, also since resolution-induced effects might behave differently for applications to data from other instruments (e.g., SOT-SP as discussed above). Actually, a robust understanding of resolution-induced effects from the application of the optimization method (and actually of that of other existing NLFF methods) to SOT-SP data is not existing to date.

Another aspect to consider is the following. Trends detected from the time series of qualifying solutions, in terms of systematic increases or decreases along individual time series, appear consistent across different resolutions, including flare-related changes of magnetic energies and helicities (Figs. 4 and 5). The magnitude of those changes is decreasing with decreasing resolution, however. For instance, taking the last/first available data point prior/after the start/end of the nominal flare impulsive phase, we find from bin[1,2,4]-based modeling flare-related changes of $\Delta E_{\rm F}\approx[25.7, 21.4, 9.6]\%$ for the X2.2 flare hosted by AR 11158, $\Delta E_{\rm F}\approx[27.9, 25.6, 21.2]\%$ for the X5.4 flare hosted by AR 11429, and $\Delta E_{\rm F}\approx[38.4, 32.9, 31.3]\%$ for the X2.2 flare hosted by AR 12673. (Due to the lack of qualifying NLFF solutions, a corresponding estimate for the X9.3 flare cannot be provided.) Similar tendencies can be deduced for the flare-related changes of, e.g., $H_{\rm J}$. These findings indicate that the binning of data prior to NLFF modeling lowers (thus, possibly underestimates) the estimates of flare-related changes, due to the model magnetic fields being naturally more similar to each other than if they were based on higher-resolution data (due to the smoothing of possibly important magnetic flux and electric currents at small spatial scales).

More generally, the realism of any kind of modeling is usually assumed to increase if the truly involved spatial scales are accommodated adequately. In other words, modeling at higher spatial resolution is assumed to provide a better representation of the true complexity of the static magnetic corona. In Fig. 8 we visualize NLFF magnetic field models at different spatial resolutions, exemplary for AR 12673 at 08:48 on 2017 September 6. Despite exhibiting some differences in morphology, the models at all of the three tested spatial resolutions reveal essentially the same basic connectivity within the AR core, including the strongly twisted field along of the solar north-south direction in the eastern part of the AR (see also, e.g., Moraitis et al. 2019, for the visualization of morphological differences when using different free model parameters during optimization). Then, it remains to be judged from case to case and based on a corresponding in-depth analysis of the magnetic field morphology, whether or not its inherent spatial resolution is sufficient to provide model support for specific observed features.

Finally, to place all of the above into greater context, the overall changes induced by a change in spatial resolution are small compared to those possibly induced by usage of different calibration products of a given instrument or the usage of data from different instruments. For such cases, relative changes for the unsigned magnetic fluxes and magnetic energies by factors of $\gtrsim 2$ were reported (Thalmann et al. 2012, 2013). Also differences arising from the application of different NLFF methods to the very same data set appear much larger, with method-induced differences of by factors of $\gtrsim 2$ for free energy estimates (DeRosa et al. 2015).

5. Summary and Conclusion

NLFF modeling is regularly used in order to indirectly infer the 3D geometry of the coronal magnetic field, not accessible on a regular basis by means of direct measurements otherwise. For such purposes, routinely measured photospheric magnetic field vector data binned to a coarser spatial resolution are used as an input. This practice, however, was suspected to affect the reliability of the modeling (DeRosa et al. 2009). In a dedicated study that analyzes the resolution-dependence of different NLFF methods, DeRosa et al. (2015) demonstrated indeed non-negligible effects. That work, however, was based on the analysis of NLFF modeling based on of vector magnetic field data at a single time instant. Thus, it remained unclear whether or not detected trends are to be expected in general. Moreover, spatial-resolution induced variations were difficult to interpret against method-induced ones, since different NLFF methods tested in that work treat the input data very differently.

In this work, we aimed at partially closing those gaps. In order to study resolution-induced effects systematically, we performed multi-snapshot NLFF modeling using a single NLFF

(optimization; Wiegelmann et al. 2012) method. For three solar ARs (NOAAs 11158, 11429, and 12673), we used time series of SDO/HMI data at three different spatial resolutions: once at their native resolution, and reduced by factors of two and four. This allowed us, 1) to study the effect of binning as a function of time (within time series of individual ARs), 2) to spot very different resolution-induced changes for different ARs, and 3) to deduce general trends.

Regarding items 1) and 2) above, we clearly demonstrated that a certain change in spatial resolution does not necessarily translate to similar effects at another time instant within a time series of NLFF models for a particular AR, and also that the induced changes can be distinctly different for different ARs. This is true for, both, the magnitude of the induced changes as well as the their "direction" (increasing or decreasing). From the detailed analysis of the different-resolution HMI data-based NLFF model time series of particularly chosen ARs, we found that:

1. The overall success of NLFF modeling at a given spatial resolution (plate scale) is necessarily different for different ARs, but also varies considerably across the model time series of individual ARs (Sect. 3.1). Thus, in agreement with past experience, concise quality checks are to be performed for every single NLFF model, prior to any attempt to interpret deduced physical parameters.

2. Among frequently used metrics to quantify of the solenoidal quality of NLFF models two measures deduced from magnetic energy decomposition appear most sensitive (thus indicative), namely the fraction of non-solenoidal contributions to the total energy (E_{div}/E) and the relative size of non-solenoidal and free magnetic energy ($|E_{\mathrm{mix}}|/E_{\mathrm{J},s}$). The recently proposed measure $\langle|f_d|\rangle$ appears less sensitive in that respect.

3. The solenoidal quality of a NLFF model neither relates to the underlying spatial resolution, nor is to be found at similar levels for different ARs even when given the same underlying spatial resolution (Sect. 3.1 and Fig. 2).

4. Binning of SDO/HMI data by a factor of four (to a plate scale of ~1.44 Mm (our "bin4" case) are may yield unphysical solutions (for which $E_F < 0$; see Sect. 3.2.2 and Fig. 4).

5. The ultimate controlling parameter of the resolution-induced variations of the deduced physical quantities is the solenoidal quality of the NLFF model. This is evidenced by a corresponding obvious (1:1) relation of both, resolution-induced changes to amplitudes as well as to temporal patterns, in parts clearly differing form those seen in the respective input data.

6. For each of our tested ARs, comparatively larger values of E, E_F, and $|H_J|$, in conjunction with lower values of E_0, $|H_V|$, and $|H_{\mathrm{PJ}}|$ (Sect. 3.2.2 and 3.2.3) were found for models with lower values of $|E_{\mathrm{mix}}|/E_{\mathrm{J},s}$ (and to a large degree also lower values of E_{div}/E).

7. Despite fluctuations, observed trends in the time series of the model-deduced physical parameters for the individual ARs appear consistent across different resolutions, including, e.g., phases of systematic increases or decreases and pronounced flare-related changes.

Having our extended analysis at hand, we were also able to deduce some general trends for the application to HMI data (cf. Sect. 4):

1. Using $\langle\theta_J\rangle$, E_{div}/E and $|E_{\mathrm{mix}}|/E_{\mathrm{J},s}$ as measures, NLFF model quality tends to be higher at reduced spatial resolution (Fig. 6). Taken together with larger values of E, E_F and H_J

(Fig. 7) hint at the optimization method to converge to more satisfactory solutions at lower spatial resolutions.

2. Estimates of flare-related changes of E_F and H_J from NLFF modeling at lower resolutions are found systematically smaller, i.e., possibly underestimate the true extent.

3. Binning of SDO/HMI data by a factor of two (to a plate scale of ~0.72 Mm; "bin2") yields changes to the deduced volume-integrated magnetic energies, E_0 and E, of $\lesssim 5\%$ and to the relative helicities, H_V and H_{PJ}, of $\lesssim 10\%$ (Fig. 7). Only for E_F and H_J they are somewhat larger ($\approx 20\%$).

4. NLFF modeling at different spatial resolutions yield consistent results on the basic magnetic connectivity of an analyzed solar AR (Fig. 8). To which extent NLFF modeling at a specific spatial resolution is suited to provide model support for selected observational features remains to be demonstrated and evaluated independently for any employed model.

5. Resolution-induced changes appear relatively small compared to other possible sources of uncertainty, including effects related to the usage of different calibration products, usage of input data from different instruments, or the application of different NLFF methods.

References

Berger, M. A. 1999, Plasma Physics and Controlled Fusion, 41, B167
Berger, M. A. 2003, Topological quantities in magnetohydrodynamics, ed. A. Ferriz-Mas & M. Núñez, 345–374
Berger, M. A. & Field, G. B. 1984, Journal of Fluid Mechanics, 147, 133
Bobra, M. G., Sun, X., Hoeksema, J. T., et al. 2014, Sol. Phys., 289, 3549
Cargill, P. J. 2009, Space Sci. Rev., 144, 413
DeRosa, M. L., Schrijver, C. J., Barnes, G., et al. 2009, ApJ, 696, 1780
DeRosa, M. L., Wheatland, M. S., Leka, K. D., et al. 2015, ApJ, 811, 107
Finn, J. & Antonsen, T. J. 1984, Comments Plasma Phys. Controlled Fusion, 9, 111
Fuhrmann, M., Seehafer, N., Valori, G., & Wiegelmann, T. 2011, A&A, 526, A70
Gary, G. A. 2001, Sol. Phys., 203, 71
Gary, G. A. & Hagyard, M. J. 1990, Sol. Phys., 126, 21
Gilchrist, S. A., Leka, K. D., Barnes, G., Wheatland, M. S., & DeRosa, M. L. 2020, ApJ, 900, 136
Gupta, M., Thalmann, J. K., & Veronig, A. M. 2021, A&A, 653, A69
Linan, L., Pariat, É., Moraitis, K., Valori, G., & Leake, J. 2018, ApJ, 865, 52
Lites, B. W., Akin, D. L., Card, G., et al. 2013, Sol. Phys., 283, 579
Metcalf, T. R., Jiao, L., McClymont, A. N., Canfield, R. C., & Uitenbroek, H. 1995, ApJ, 439, 474
Moffatt, H. K. 1969, Journal of Fluid Mechanics, 35, 117
Moraitis, K., Sun, X., Pariat, É., & Linan, L. 2019, A&A, 628, A50
Pesnell, W. D., Thompson, B. J., & Chamberlin, P. C. 2012, Sol. Phys., 275, 3
Régnier, S. 2013, Sol. Phys., 288, 481
Scherrer, P. H., Schou, J., Bush, R. I., et al. 2012, Sol. Phys., 275, 207
Thalmann, J. K., Inhester, B., & Wiegelmann, T. 2011, Sol. Phys., 272, 243
Thalmann, J. K., Linan, L., Pariat, E., & Valori, G. 2019, ApJ, 880, L6
Thalmann, J. K., Pietarila, A., Sun, X., & Wiegelmann, T. 2012, AJ, 144, 33
Thalmann, J. K., Sun, X., Moraitis, K., & Gupta, M. 2020, A&A, 643, A153
Thalmann, J. K., Tiwari, S. K., & Wiegelmann, T. 2013, ApJ, 769, 59
Tsuneta, S., Ichimoto, K., Katsukawa, Y., et al. 2008, Sol. Phys., 249, 167
Valori, G., Démoulin, P., & Pariat, E. 2012, Sol. Phys., 278, 347
Valori, G., Démoulin, P., Pariat, E., & Masson, S. 2013, A&A, 553, A38
Valori, G., Pariat, E., Anfinogentov, S., et al. 2016, Space Sci. Rev., 201, 147
Wheatland, M. S. & Leka, K. D. 2011, ApJ, 728, 112
Wheatland, M. S. & Régnier, S. 2009, ApJ, 700, L88
Wheatland, M. S., Sturrock, P. A., & Roumeliotis, G. 2000, ApJ, 540, 1150
Wiegelmann, T. & Inhester, B. 2010, A&A, 516, A107
Wiegelmann, T., Inhester, B., & Sakurai, T. 2006, Sol. Phys., 233, 215
Wiegelmann, T., Petrie, G. J. D., & Riley, P. 2017, Space Sci. Rev., 210, 249
Wiegelmann, T. & Sakurai, T. 2012, Living Reviews in Solar Physics, 9, 5
Wiegelmann, T., Thalmann, J. K., Inhester, B., et al. 2012, Sol. Phys., 281, 37